

A Fluid-Structure Interaction Model of the Zebrafish Aortic Valve

Alexander D. Kaiser,^{1,2} Jing Wang,³
Aaron L. Brown,^{2,4} Enbo Zhu,⁵
Tzung Hsiai,^{3,5} & Alison L. Marsden,^{2,6,7,8}

December 25, 2024

¹Department of Cardiothoracic Surgery, Stanford University, Stanford CA;

²Stanford Cardiovascular Institute, Stanford CA;

³Department of Bioengineering, University of California, Los Angeles, Los Angeles, CA;

⁴Department of Mechanical Engineering, Stanford University, Stanford CA;

⁵Division of Cardiology, Department of Medicine, School of Medicine, University of California, Los Angeles, Los Angeles, CA;

⁶Department of Pediatrics (Cardiology), Stanford University, Stanford CA;

⁷Department of Bioengineering, Stanford University, Stanford CA;

⁸Institute for Computational and Mathematical Engineering, Stanford University, Stanford CA

Abstract

The zebrafish is a valuable model organism for studying cardiac development and diseases due to its many shared aspects of genetics and anatomy with humans and ease of experimental manipulations. Computational fluid-structure interaction (FSI) simulations are an efficient and highly controllable means to study the function of cardiac valves in development and diseases. Due to their small scales, little is known about the mechanical properties of zebrafish cardiac valves, limiting existing computational studies of zebrafish valves and their interaction with blood. To circumvent these limitations, we took a largely first-principles approach called *design-based elasticity* that allows us to derive valve geometry, fiber orientation and material properties. In FSI simulations of an adult zebrafish aortic valve, these models produce realistic flow rates when driven by physiological pressures and demonstrate the spatiotemporal dynamics of valvular mechanical properties. These models can be used for future studies of zebrafish cardiac hemodynamics, development, and disease.

1 Introduction

The zebrafish is a widely used model organism to study cardiac development and diseases, sharing 82% of disease-associated genes with humans, including 96% of dilated cardiomyopathy (DCM) genes (Howe et al., 2013; Shih et al., 2015). The zebrafish provides unique advantages in high-throughput experiments via its translucent body during the embryonic stage that permits *in vivo* imaging, short gestational period and time to maturity. The zebrafish has a two-chambered heart with two valves, in contrast to four chambers with four valves in humans. The heart possesses one atrium, an atrioventricular (AV) valve, one ventricle, an outflow structure called the bulbus arteriosus, and a semilunar aortic (outflow tract or OFT) valve in the outflow tract. The aortic valve is bicuspid, with two leaflets of approximately equal size and shape. This valve resembles a rare congenitally diseased phenotype that occurs in humans, a Sievers Type 0 bicuspid valve that has

no raphe (Sievers and Schmidtke, 2007). Computational fluid dynamics (CFD), including fluid-structure interaction (FSI) simulations, has facilitated uncovering novel mechanisms underlying the zebrafish cardiac morphogenesis (Salman and Yalcin, 2020). While the FSI simulations of endocardial wall elucidated shear-stress mediated valvular development, successful attempts to simulate valve-fluid interaction in zebrafish have not been documented (Hsu et al., 2019). Moreover, the mechanical properties of the zebrafish aortic valve are poorly understood and difficult to directly measure because of its small size.

In this work, we constructed a computational model of an adult zebrafish aortic valve and conducted FSI simulations to model its interaction with blood. Due to the lack of information on the gross morphology of the valve and its material properties, as well as our previous successes with the method, we applied a nearly first-principles approach that we refer to as *design-based elasticity*. In this approach, we derived a system of partial differential equations to represent the closed valve as it supports a pressure load. The solution to these equations was then used to derive the material properties, fiber orientation, and reference configuration of the model valve. By tuning parameters in these equations, we designed the valve to achieve realistic flow rates and closure when driven by physiological pressures.

Initially developed to model the human mitral valve (Kaiser et al., 2019), we have previously applied design-based elasticity to the human aortic valve (Kaiser et al., 2021). We studied the effect of phenotype on hemodynamics in Sievers Type 1 bicuspid valves (Kaiser et al., 2022) and showed that model flows compared well to an *in vitro* experiment measured with flow with 4D flow Magnetic Resonance Imaging (4DMRI) (Kaiser et al., 2023). We conducted initial simulation-guided design studies of bicuspidization repair of the aortic valve (Kaiser et al., 2024) and validated predicted trends in pressure gradient *in vitro* (Choi, Sharir, Ono, Shibata, Kaiser, Zhu, Marsden, Woo, Ma and Kim, 2024; Choi, Sharir, Ono, Shibata, Kaiser, Palagani, Marsden and Ma, 2024). Our methods have thus proven effective for modeling a variety of flows involving heart valves and compare well to experimental data, and thus are appropriate for modeling the zebrafish valve.

Other FSI studies have examined flow in the developing heart (Battista et al., 2018; Hsu et al., 2019; Lee et al., 2013, 2018; Vedula et al., 2017), including one study with simplified two-dimensional endocardial cushions that develop into valves (Miller, 2011), and adult vasculature (Van Impe et al., 2023).

To our knowledge this is the first study to perform three-dimensional FSI on the zebrafish valve. Our model produced realistic flow rates and robust closure in diastole over multiple cardiac cycles. This study serves as a proof of concept towards future studies of the mechanisms of zebrafish valve function, disease and development.

2 Methods

2.1 Imaging and Anatomy

A schematic together with light-sheet images of the zebrafish heart is shown in Figure 1. The clearing of the 1 year-old Tg(TP1:EGFP) (Parsons et al., 2009) zebrafish heart was carried out following a CUBIC-based protocol from Tokyo Chemical Industry (TCI) (Tainaka et al., 2018). Briefly, the heart was washed in PBS before undergoing serial incubations in CUBIC-L (TCI, T3740) and CUBIC-R+(M) (TCI, T3741) solutions at room temperature. Finally, the cleared heart was immersed in the mounting solution (TCI, M3294, RI = 1.520) and imaged using a customized light-sheet system at 6.3X magnification. Adult zebrafish were raised and bred in the UCLA Zebrafish Core Facility according to standard protocols (Westerfield, 2007). All experiments

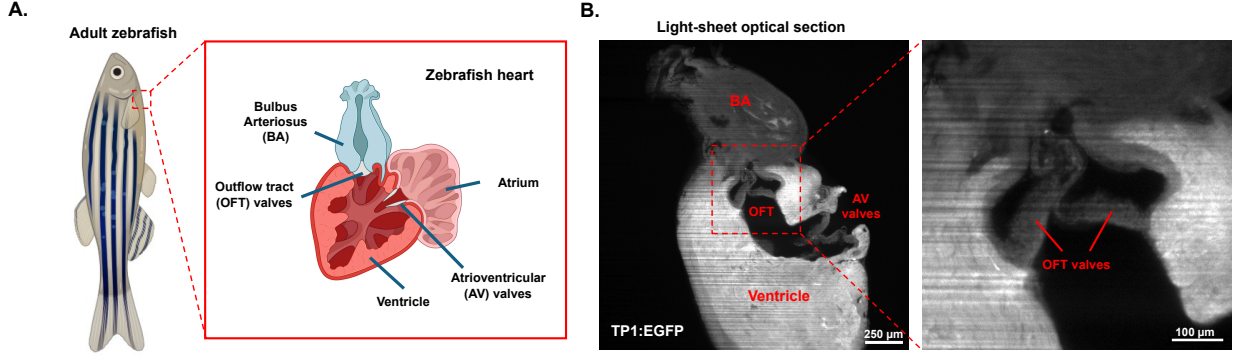


Figure 1: Anatomy of zebrafish heart and light-sheet optical section of OFT (aortic) valves. A. Illustration of the adult zebrafish and its cardiac structure. B. Light-sheet imaging of a cleared 1 year-old zebrafish heart showing the AV and OFT valves.

with zebrafish were performed in compliance with and with the approval of a UCLA Institutional Animal Care and Use Committee protocol (ID: ARC-2015-055).

2.2 Model construction

Models were constructed with a nearly first-principles method called design-based elasticity that we previously applied to model the human aortic valve (Kaiser et al., 2021). The methods are briefly summarized here with changes for the zebrafish highlighted.

First, we assumed that tension in the leaflets supported a static, uniform pressure load p . The leaflet was represented as an unknown parametric surface $\mathbf{X}(u, v) : \Omega \subset \mathbb{R}^2 \rightarrow \mathbb{R}^3$, where curves of constant v run circumferentially and curves of constant u run radially. The leaflets exerted tension S circumferentially, corresponding to the anatomical fiber direction, and tension T radially, corresponding to the cross-fiber direction. We specified that tension on the boundary of an arbitrary patch of leaflet balanced pressure, applied the fundamental theorem of calculus to convert boundary terms to surface terms, then finally dropped the integrals as the region of interest was arbitrary. Let single bars, $|\cdot|$, denote the Euclidean norm and subscripts denote partial derivatives. We thus obtained the following system of partial differential equations that represent the predicted, loaded configuration of the leaflets,

$$0 = p(\mathbf{X}_u \times \mathbf{X}_v) + \frac{\partial}{\partial u} \left(S \frac{\mathbf{X}_u}{|\mathbf{X}_u|} \right) + \frac{\partial}{\partial v} \left(T \frac{\mathbf{X}_v}{|\mathbf{X}_v|} \right). \quad (1)$$

We then assigned the following tension law for S and T ,

$$S(u, v) = \alpha \left(1 - \frac{1}{1 + |\mathbf{X}_u|^2/a^2} \right), \quad T(u, v) = \beta \left(1 - \frac{1}{1 + |\mathbf{X}_v|^2/b^2} \right), \quad (2)$$

where α and β control the maximum tension in each material direction, and a and b control spacing of the mathematical fibers in the model. Expression (2) acts, colloquially, as a “mathematical search function,” that allowed the solution to find a heterogenous field of tensions that support the specified load.

To design a realistic model for a zebrafish, the pressure p was set to 0.92 mmHg, the mean pressure difference across the valve when the aortic pressure was greater than the ventricular pressure (Hu et al., 2001). The model was set to have two symmetrical leaflets, each subtending

half the annular circumference. The valve diameter was set to 363 microns and commissure height to 285 microns, based on measurements from a light-sheet image of the valve (Fig. 1B). This imaging modality allowed viewing of the annulus, but was highly collapsed and compressed since the fish was deceased at the time of imaging. Thus, these are low estimates on the valve radius and height, but were used due to lack of comparable *in vivo* data. The parameters that control the maximum tension were set to $\alpha = 4.1 \cdot 10^5$ and $\beta = 1.4 \cdot 10^4$ dynes. The spacing parameter a varied linearly from $a = 26.2 - 100$ cm from the annulus to the free edge, and the parameter $b = 40$ cm. These parameters were designed by trial and error to produce a model free edge length (leaflet width) of 571 microns in the reference configuration, or approximately 1.57 times the annular diameter, as in previous work on bicuspidization repair of the aortic valve (Kaiser et al., 2024). The resultant leaflet height (or geometric height) was 169 microns in the reference configuration.

To derive a constitutive law from the predicted, loaded configuration, we prescribed uniform stretch of $\lambda_c = 1.15$ and $\lambda_r = 1.54$ circumferentially and radially (Yap et al., 2009). We derived the reference length R for all links in the discretized model via solving the equation $\lambda = L/R$, where λ is the relevant stretch and L is the current length of a given edge or “link” in the discretized model. Each link was set to take an exponential response with exponential rate taken from experimental data (May-Newman et al., 2009). The stiffness of each link was then scaled to take the tension required in the solution of the equilibrium equations (1) at the prescribed stretches. To obtain an open initial configuration, an additional equilibrium equation was solved with $p = 0$ mmHg and the constitutive law just derived. Finally, two additional membranous layers were added to create a model thickness of 6.3 microns, which was scaled proportionally to valve radius from our previous models (Kaiser et al., 2021). (Note that image resolution in the out of plane direction may cause the leaflets in Fig. 1B to appear artificially thicker than they are, and thus thickness was not assessed from this image.) The layers were attached to each other with stiff linear springs, and the stiffnesses of each membrane layer were set to one third of the initial stiffnesses across the three layers. The model was fully fiber-based, in that all circumferential, radial and cross-layer forces are computed along fibers, curves that exert tension along their axis. Links that were longer than twice the fluid mesh width were split and assigned the same relative spring constant. Stretch, stress and tangent modulus from FSI simulations were computed from the original membranous layer on the aortic side of the leaflet. This model construction resulted in a mean tangent modulus in the predicted loaded configuration of $2.83 \cdot 10^6$ dynes/cm² circumferentially and $1.16 \cdot 10^5$ dynes/cm² radially.

2.3 Fluid-Structure Interaction

Fluid-structure interaction simulations were performed with the Immersed Boundary Method (Peskin, 2002) in the open-source solver IBAMR (Immersed Boundary Adaptive Mesh Refinement) (Griffith et al., 2010). The fluid mesh width was set to 5 microns. The time step was set to $5 \cdot 10^{-7}$ s, which was extremely restrictive, due to very small spatial resolution and only modestly lower stiffness compared to human data. The valve was placed into a cylindrical tube of length 1.28 mm with diameter 363 microns with a flow extender at the inlet of length 150 microns and an additional radius 50 microns.

The cardiac cycle duration was 0.32 s, or approximately 185 beats per minute (Hu et al., 2001) and simulations were run for two cycles. The first cycle was discarded due to initialization effects and results from the second cycle are shown. Times are reported from the start of the second cycle. The ventricular pressure was prescribed at the upstream inlet based on experimental measurements (Hu et al., 2001), which were smoothed via convolution with a normalized cosine bump of radius .025 s and represented as a finite Fourier series with 600 frequencies.

The aortic outlet pressure was governed via a RCR (resistor capacitor resistor) lumped parameter network that models the distal vasculature, following a brief initialization phase. The minimum, maximum and mean aortic pressure were estimated to be 0.89, 2.08 and 1.39 mmHg respectively (Hu et al., 2001). The flow rate target was set to 266 nl (Van Impe et al., 2023). The ratio of proximal to distal resistors was set to 0.065 via an experimental estimate in humans, as we lack a value of this ratio for the zebrafish (Laskey et al., 1990). The values were then estimated via the method previously described (Kaiser et al., 2021). This process resulted in values $R_p = 1.3 \cdot 10^4$ dynes cm^{-5} , $R_d = 2.1 \cdot 10^6$ s dynes cm^{-5} and $C = 1.0 \cdot 10^{-7}$ cm^5 dynes $^{-1}$ for proximal resistance, distal resistance and capacitance, respectively.

3 Results

The valve shows unrestricted forward flow during systole and robust closure during diastole over multiple cardiac cycles (Fig. 2). The velocity field showed no evidence of regurgitation and low magnitude flow during closure. Twist was visible in the closed configuration, indicating presence of excess free edge length during diastole. The leaflets showed no billow or prolapse. The valve opens to nearly the radius of the cylindrical test chamber, indicating sufficient free edge length for maximal orifice area during systole. The forward flow is highly laminar, without any appearance of vortices or instabilities in the flow. When the flow rate nears zero, the local velocity is also low-magnitude while the valve remains open. The closing transient appears roughly symmetric, with a transient crease in both leaflets. Finally, the valve again fully closes with slight twist and no appearance of regurgitation. The flow dynamics are further depicted in the movie included with the supplemental information.

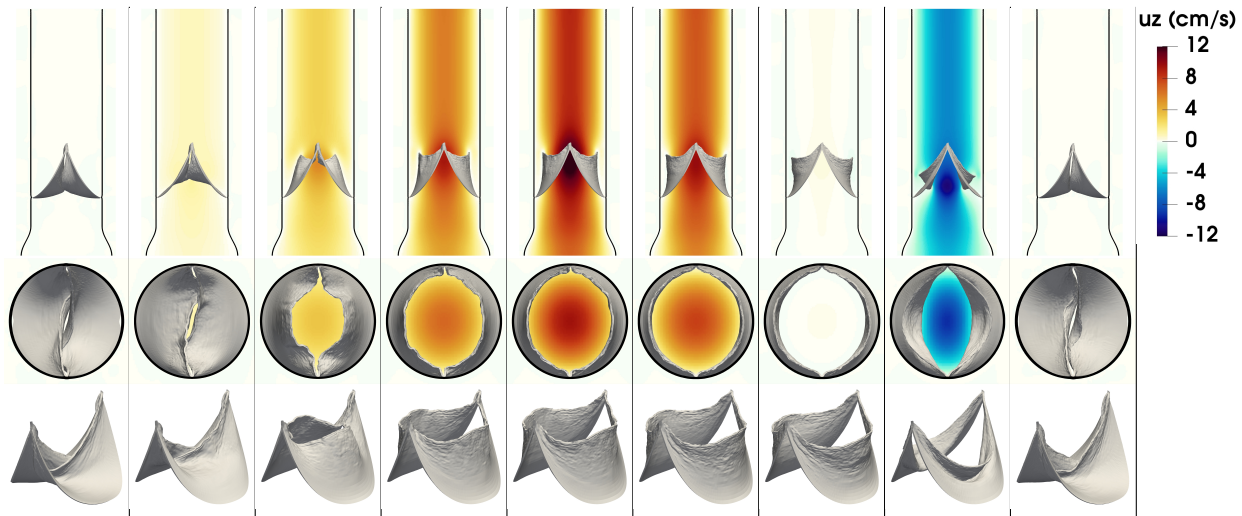


Figure 2: Flows through the cardiac cycle, depicting a slice view of the vertical component of velocity u_z with a side view of the valve (top row), the valve viewed *en face* (middle row) and the valve viewed at an angle (bottom row).

Pressure and flow rate waveforms showed approximately physiological values (Hu et al., 2001; Van Impe et al., 2023) through the cardiac cycle (Fig. 3). The aortic pressure resulted from the coupled dynamics of the full FSI system and the RCR boundary conditions. The pressure lowered gradually through end diastole, rose with systole, showed a prominent dicrotic notch upon valve closure, then again began to decrease gradually during diastole. The aortic pressure took

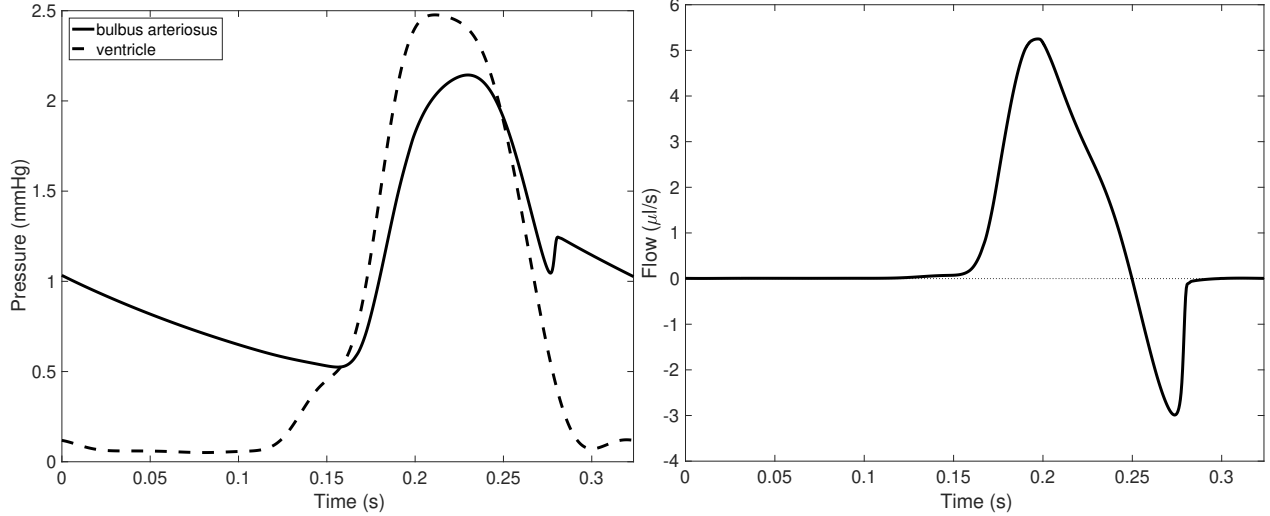


Figure 3: Pressure and flow waveforms.

minimum, maximum and mean values of 0.52, 2.14 and 1.10 mmHg, respectively. Across the valve (and including the surrounding test chamber), the peak pressure gradient was 0.62 mmHg and mean gradient was 0.34 mmHg. The flow rate was near zero during diastole, then showed rapid increase with forward pressure, followed by sustained forward flow. After the pressure difference changed sign, the flow rate shows a transient of backflow. The majority of this was likely blood that has not fully passed the leaflet free edge. The valve returned to its closed state, and the flow rate settled around zero without regurgitation.

The stroke volume was 266 nl and stroke volume minus retrograde volume (nearly all from the closing transient) was 209 nl. The maximum flow rate was $Q_{max} = 5.25 \mu\text{l/s}$. The mean systolic flow was $Q_{mean} = 2.85 \mu\text{l/s}$, which was computed between the time at which the pressure difference across the valve turned positive to the time at which the flow rate turned negative. The maximum Reynolds number was $Re_{max} = \rho(Q_{max}/A)r/\mu = 2.30$ and the mean Reynolds number was $Re_{mean} = \rho(Q_{mean}/A)r/\mu = 1.25$, where A denotes the cross sectional area of the test chamber. The Reynolds number is thus order one and the flow lies in an intermediate regime, neither Stokes flow nor a fully inertial regime.

The stretch, stress and tangent modulus were anisotropic and generally higher in diastole when the valve is closed (Fig. 4). In diastole, the circumferential stretch was near to the predicted loaded stretch, which is expected by construction, away from the free edge. The stretch was lower in the coapted region where the valve is presumably less loaded circumferentially. The stress and tangent modulus showed a concentration of stress and tangent modulus near the commissure. Stresses were more modest in the belly of the leaflet, and lower still at the free edge. The radial stretch, stress and tangent modulus were higher near the annulus and lower towards the free edge. The mean values of circumferential stretch, stress and tangent modulus were 1.12, $2.36 \cdot 10^4$ dynes/cm² and $1.36 \cdot 10^6$ dynes/cm², respectively. The mean values of radial stretch, stress and tangent modulus were 1.44, $4.09 \cdot 10^3$ dynes/cm² and $9.16 \cdot 10^4$ dynes/cm², respectively.

In systole, the circumferential stretch, stress and tangent modulus are much lower than in diastole, as expected with much less pressure loading on the valve. The stretch was higher near the annulus and decreased towards the free edge, and stress and tangent modulus were correspondingly lower. Radially, more stretch remained during forward flow, likely due to axially aligned shear on the valve. Elevated radial stress and tangent modulus were observed near the annulus, with more

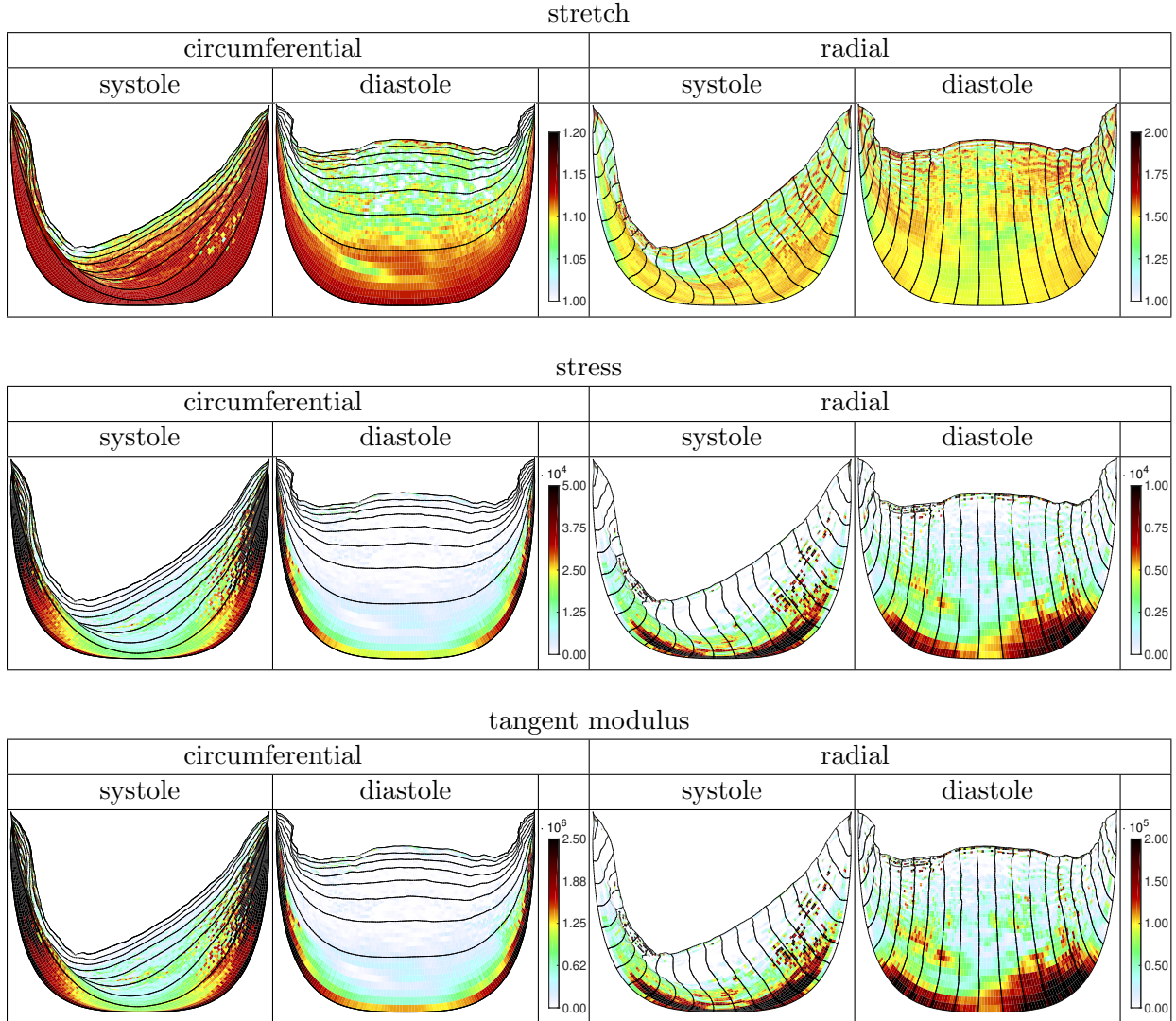


Figure 4: Stretch, stress (dynes/cm²) and tangent modulus (dynes/cm²) circumferentially and radially in systole and diastole. Note differing scales throughout the figure.

modest stress and tangent modulus through the leaflet belly.

4 Discussion and Conclusions

In this work, we have constructed a model of the zebrafish aortic valve using a first principles approach. These methods allowed for estimates of material properties of zebrafish valvular tissue that are largely unknown. In FSI simulations under physiological pressures, the model showed realistic kinematics and flow rates. These appear to be the first three-dimensional FSI simulations of the zebrafish aortic valve.

This work shows interesting scalings and similarities compared to human values. The cardiac cycle duration is less than one order of magnitude shorter than that of humans. Approximately, valve diameter is lower by two orders of magnitude, pressure is lower by two orders of magnitude, velocity is lower by one order of magnitude, stroke volume and flow rate are lower by five orders of

magnitude, and Reynolds number is lower by three orders of magnitude, compared to corresponding values in humans. This lower Reynolds number resulted in highly laminar flow patterns with no vortices visible in the velocity field, in stark contrast to human flows that show inertial effects including unsteady flow, vortices, and small regions of recirculation (even in the trileaflet case) (Kaiser et al., 2022).

The leaflet kinematics also showed similarities, with some notable contrasts, to human studies. The qualitative kinematics were strikingly similar to those we observed in previous simulations, with similar appearance of the open configuration and orifice, as well as the closed configuration including appearance of slight excess free edge tissue (Kaiser et al., 2024). One notable difference was the closing transient, which showed a single negative oscillation, rather than a sustained oscillation with multiple sign changes in flow rate, that appeared proportionally longer in duration than that we observed in previous human simulation studies. It has been hypothesized and shown that vortices shed from the leaflet and in the aortic sinus assist in human aortic valve closure (Bellhouse and Talbot, 1969). Given the Reynolds number and lack of vortices or a sinus, this mechanism does not occur in our simulations of the zebrafish valve, but the valve closes without leak nonetheless. This work thus suggests that while vortices may assist closure, this mechanism is not necessary for valve closure. The vortex, however, may shorten the closing transient and reduce associated regurgitant flow.

Examining leaflet mechanics, experimental estimates on human valves predicted a tangent modulus of $9.9 \pm 1.8 \cdot 10^7$ dynes/cm² circumferentially and $2.3 \pm 0.4 \cdot 10^7$ dynes/cm² radially (Pham et al., 2017). Thus, the predicted tangent moduli in the zebrafish are two orders of magnitude lower than that of humans. Other studies were qualitatively similar to our results. A combined experimental/simulation study showed elevated stress at the commissures and somewhat elevated stress in the leaflet belly (Balguid et al., 2008). Another combined experimental/simulation study showed elevated radial stretch near the annulus, decreasing into the leaflet belly and lower still near the free edge, and elevated circumferential stretch and in the leaflet belly (Rego et al., 2022).

The anisotropic stress field in mammalian aortic valve arises from its unique extracellular matrix (ECM) architecture that comprises of 3 layers: a fibrosa layer rich in circumferential collagen fibers facing the aortic side, a spongiosa middle layer rich in proteoglycans, and a ventricularis layer rich in radial elastin fibers facing the ventricular side (Billiar and Sacks, 2000; Gould et al., 2013; Kodigepalli et al., 2020). Moreover, the fibers near the commissure have the largest diameters and the lowest density, while the fibers near the fixed edge of mid-annulus are thin and high in density (Balguid et al., 2008). Although a direct mechanical characterization of zebrafish aortic valves has not been possible, histological analysis indicates that they contain a similar elastin- and collagen-rich ventricularis-like layer and a proteoglycan-rich spongiosa-like layer (Schulz et al., 2019). However, the fibrosa layer does not seem to exist, and the leaflets are much more cellular compared to the mammalian leaflets. As the spatial organization of ECM components plays a critical role in valvular functions, our method provides a useful tool for researchers to assess the structural and mechanical remodeling of leaflets when studying zebrafish disease models (Chen and Simmons, 2011).

This study has limitations, in particular we lack experimental measurements of material properties and *in vivo* valve geometry to validate our predictions. The test chamber is a cylindrical shape, rather than a beating heart or anatomical shape due to lack of *in vivo* images at this developmental timepoint. We relied on an *ex vivo* image of the zebrafish heart that was collapsed without pressure for estimating annular radius and height.

To conclude, our modeling methods produce model geometry, fiber structure and material properties from nearly first principles that showed realistic behavior in FSI simulations. These methods can thus be utilized for further studies of heart valves and their surrounding hemodynamics

in the zebrafish. These findings serve as a basis for future studies on valve development and function in a commonly used model of cardiac development.

5 Acknowledgements

All authors were supported in part by NIH grants 5R01HL129727-08 and 5R01HL159970-04. EZ was supported in part by NIH grant T32HL144449 Computing for this project was performed on the Stanford University’s Sherlock cluster with assistance from the Stanford Research Computing Center. We would like to thank David Traver (UCSD) and Nathan Lawson (University of Massachusetts Medical School) for providing the fish line.

References

- Balguid, A., Driessen, N. J., Mol, A., Schmitz, J. P., Verheyen, F., Bouten, C. V. and Baaijens, F. P. (2008). Stress related collagen ultrastructure in human aortic valves—implications for tissue engineering, *Journal of biomechanics* **41**(12): 2612–2617.
- Battista, N. A., Lane, A. N., Liu, J. and Miller, L. A. (2018). Fluid dynamics in heart development: effects of hematocrit and trabeculation, *Mathematical medicine and biology: a journal of the IMA* **35**(4): 493–516.
- Bellhouse, B. J. and Talbot, L. (1969). The fluid mechanics of the aortic valve, *Journal of fluid mechanics* **35**(4): 721–735.
- Billiar, K. L. and Sacks, M. S. (2000). Biaxial mechanical properties of the natural and glutaraldehyde treated aortic valve cusp—part i: experimental results, *J. Biomech. Eng.* **122**(1): 23–30.
- Chen, J.-H. and Simmons, C. A. (2011). Cell–matrix interactions in the pathobiology of calcific aortic valve disease: critical roles for matricellular, matricrine, and matrix mechanics cues, *Circulation research* **108**(12): 1510–1524.
- Choi, P. S., Sharir, A., Ono, Y., Shibata, M., Kaiser, A. D., Palagani, Y., Marsden, A. L. and Ma, M. R. (2024). Combined simulation and ex-vivo assessment of free-edge length in bicuspidization repair for congenital aortic valve disease, *The Journal of Thoracic and Cardiovascular Surgery Open* .
- Choi, P. S., Sharir, A., Ono, Y., Shibata, M., Kaiser, A. D., Zhu, Y., Marsden, A. L., Woo, Y. J., Ma, M. R. and Kim, J. B. (2024). Effect of graft sizing in valve-sparing aortic root replacement for bicuspid aortic valve: The goldilocks ratio, *JTCVS techniques* **25**: 1–7.
- Gould, S. T., Srigunapalan, S., Simmons, C. A. and Anseth, K. S. (2013). Hemodynamic and cellular response feedback in calcific aortic valve disease, *Circulation research* **113**(2): 186–197.
- Griffith, B. E., Hornung, R. D., McQueen, D. M. and Peskin, C. S. (2010). Parallel and adaptive simulation of cardiac fluid dynamics, *Advanced Computational Infrastructures for Parallel and Distributed Adaptive Applications* p. 105.
- Howe, K., Clark, M. D., Torroja, C. F., Torrance, J., Berthelot, C., Muffato, M., Collins, J. E., Humphray, S., McLaren, K., Matthews, L. et al. (2013). The zebrafish reference genome sequence and its relationship to the human genome, *Nature* **496**(7446): 498–503.

- Hsu, J. J., Vedula, V., Baek, K. I., Chen, C., Chen, J., Chou, M. I., Lam, J., Subhedar, S., Wang, J., Ding, Y. et al. (2019). Contractile and hemodynamic forces coordinate notch1b-mediated outflow tract valve formation, *JCI insight* **4**(10).
- Hu, N., Yost, H. J. and Clark, E. B. (2001). Cardiac morphology and blood pressure in the adult zebrafish, *The Anatomical Record: An Official Publication of the American Association of Anatomists* **264**(1): 1–12.
- Kaiser, A. D., Haidar, M. A., Choi, P. S., Sharir, A., Marsden, A. L. and Ma, M. R. (2024). Simulation-based design of bicuspidization of the aortic valve, *The Journal of Thoracic and Cardiovascular Surgery* .
- Kaiser, A. D., McQueen, D. M. and Peskin, C. S. (2019). Modeling the mitral valve, *International journal for numerical methods in biomedical engineering* **35**(11): e3240.
- Kaiser, A. D., Schiavone, N. K., Elkins, C. J., McElhinney, D. B., Eaton, J. K. and Marsden, A. L. (2023). Comparison of immersed boundary simulations of heart valve hemodynamics against in vitro 4d flow mri data, *Annals of Biomedical Engineering* pp. 1–22.
- Kaiser, A. D., Shad, R., Hiesinger, W. and Marsden, A. L. (2021). A design-based model of the aortic valve for fluid-structure interaction, *Biomechanics and modeling in mechanobiology* **20**(6): 2413–2435.
- Kaiser, A. D., Shad, R., Schiavone, N., Hiesinger, W. and Marsden, A. L. (2022). Controlled comparison of simulated hemodynamics across tricuspid and bicuspid aortic valves, *Annals of biomedical engineering* **50**(9): 1053–1072.
- Kodigepalli, K. M., Thatcher, K., West, T., Howsmon, D. P., Schoen, F. J., Sacks, M. S., Breuer, C. K. and Lincoln, J. (2020). Biology and biomechanics of the heart valve extracellular matrix, *Journal of cardiovascular development and disease* **7**(4): 57.
- Laskey, W. K., Parker, H. G., Ferrari, V. A., Kussmaul, W. G. and Noordergraaf, A. (1990). Estimation of total systemic arterial compliance in humans, *Journal of Applied Physiology* **69**(1): 112–119.
- Lee, J., Moghadam, M. E., Kung, E., Cao, H., Beebe, T., Miller, Y., Roman, B. L., Lien, C.-L., Chi, N. C., Marsden, A. L. et al. (2013). Moving domain computational fluid dynamics to interface with an embryonic model of cardiac morphogenesis, *PloS one* **8**(8): e72924.
- Lee, J., Vedula, V., Baek, K. I., Chen, J., Hsu, J. J., Ding, Y., Chang, C.-C., Kang, H., Small, A., Fei, P. et al. (2018). Spatial and temporal variations in hemodynamic forces initiate cardiac trabeculation, *JCI insight* **3**(13).
- May-Newman, K., Lam, C. and Yin, F. C. (2009). A hyperelastic constitutive law for aortic valve tissue, *Journal of biomechanical engineering* **131**(8).
- Miller, L. A. (2011). Fluid dynamics of ventricular filling in the embryonic heart, *Cell biochemistry and biophysics* **61**: 33–45.
- Parsons, M. J., Pisharath, H., Yusuff, S., Moore, J. C., Siekmann, A. F., Lawson, N. and Leach, S. D. (2009). Notch-responsive cells initiate the secondary transition in larval zebrafish pancreas, *Mechanisms of development* **126**(10): 898–912.

- Peskin, C. S. (2002). The immersed boundary method, *Acta Numerica* **11**: 479–517.
- Pham, T., Sulejmani, F., Shin, E., Wang, D. and Sun, W. (2017). Quantification and comparison of the mechanical properties of four human cardiac valves, *Acta biomaterialia* **54**: 345–355.
- Rego, B. V., Pouch, A. M., Gorman III, J. H., Gorman, R. C. and Sacks, M. S. (2022). Patient-specific quantification of normal and bicuspid aortic valve leaflet deformations from clinically derived images, *Annals of biomedical engineering* **50**(1): 1–15.
- Salman, H. E. and Yalcin, H. C. (2020). Advanced blood flow assessment in zebrafish via experimental digital particle image velocimetry and computational fluid dynamics modeling, *Micron* **130**: 102801.
- Schulz, A., Brendler, J., Blaschuk, O., Landgraf, K., Krueger, M. and Ricken, A. M. (2019). Non-pathological chondrogenic features of valve interstitial cells in normal adult zebrafish, *Journal of Histochemistry & Cytochemistry* **67**(5): 361–373.
- Shih, Y.-H., Zhang, Y., Ding, Y., Ross, C. A., Li, H., Olson, T. M. and Xu, X. (2015). Cardiac transcriptome and dilated cardiomyopathy genes in zebrafish, *Circulation: Cardiovascular Genetics* **8**(2): 261–269.
- Sievers, H.-H. and Schmidtke, C. (2007). A classification system for the bicuspid aortic valve from 304 surgical specimens, *The Journal of thoracic and cardiovascular surgery* **133**(5): 1226–1233.
- Tainaka, K., Murakami, T. C., Susaki, E. A., Shimizu, C., Saito, R., Takahashi, K., Hayashi-Takagi, A., Sekiya, H., Arima, Y., Nojima, S., Ikemura, M., Ushiku, T., Shimizu, Y., Murakami, M., Tanaka, K. F., Iino, M., Kasai, H., Sasaoka, T., Kobayashi, K., Miyazono, K., Morii, E., Isa, T., Fukayama, M., Kakita, A. and Ueda, H. R. (2018). Chemical landscape for tissue clearing based on hydrophilic reagents, *Cell reports* **24**(8): 2196–2210.
- Van Impe, M., Caboor, L., Deleeuw, V., Olbinado, M., De Backer, J., Sips, P. and Segers, P. (2023). Fluid-structure interaction modeling of the aortic hemodynamics in adult zebrafish: A pilot study based on synchrotron x-ray tomography, *IEEE Transactions on Biomedical Engineering* **70**(7): 2101–2110.
- Vedula, V., Lee, J., Xu, H., Kuo, C.-C. J., Hsiai, T. K. and Marsden, A. L. (2017). A method to quantify mechanobiologic forces during zebrafish cardiac development using 4-d light sheet imaging and computational modeling, *PLoS computational biology* **13**(10): e1005828.
- Westerfield, M. (2007). *The Zebrafish Book; A guide for the laboratory use of zebrafish (Danio rerio)*, University of Oregon Press, Eugene, OR.
- Yap, C. H., Kim, H.-S., Balachandran, K., Weiler, M., Haj-Ali, R. and Yoganathan, A. P. (2009). Dynamic deformation characteristics of porcine aortic valve leaflet under normal and hypertensive conditions, *American Journal of Physiology-Heart and Circulatory Physiology* **298**(2): H395–H405.